On: 30 July 2014, At: 03:47
Publisher: Taylor & Francis
Informa Ltd Registered in England and Wales Registered Number: 1072954 Registered office: Mortimer House, 37-41 Mortimer Street, London W1T 3JH, UK

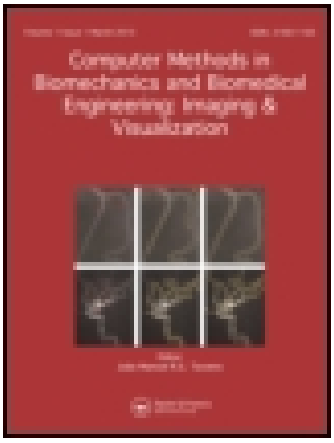

Computer Methods in Biomechanics and Biomedical Engineering: Imaging & Visualization

Publication details, including instructions for authors and subscription information:
http://www.tandfonline.com/loi/tciv20

Metal artefact reduction in computed tomography images by a fourth-order total variation flow

Elena Faggiano[ab], Tommaso Lorenzi[cde] & Alfio Quarteroni[f]

[a] Department of Mathematics, Modelling and Scientific Computing (MOX), Politecnico di Milano, Milan, Italy

[b] Laboratory of Biological Structure Mechanics (LaBs), Department of Chemistry, Material and Chemical Engineering, Politecnico di Milano, Milan, Italy

[c] Laboratoire Jacques-Louis Lions, Sorbonne Universités, UPMC Univ Paris 06, UMR 7598, F-75005 Paris, France

[d] Laboratoire Jacques-Louis Lions, CNRS, UMR 7598, F-75005 Paris, France

[e] INRIA-Paris-Rocquencourt, EPC MAMBA, Domaine de Voluceau, BP105, 78153 Le Chesnay Cedex, France

[f] Modeling and Scientific Computing (CMCS), MATHICSE, Ecole Polytechnique Fédérale de Lausanne (EPFL), Lausanne, Switzerland

Published online: 25 Jul 2014.

To cite this article: Elena Faggiano, Tommaso Lorenzi & Alfio Quarteroni (2014): Metal artefact reduction in computed tomography images by a fourth-order total variation flow, Computer Methods in Biomechanics and Biomedical Engineering: Imaging & Visualization, DOI: 10.1080/21681163.2014.940629

To link to this article: http://dx.doi.org/10.1080/21681163.2014.940629

Computer Methods in Biomechanics and Biomedical Engineering: Imaging & Visualization, 2014
http://dx.doi.org/10.1080/21681163.2014.940629

Metal artefact reduction in computed tomography images by a fourth-order total variation flow

Elena Faggiano[a,b]*, Tommaso Lorenzi[c,d,e] and Alfio Quarteroni[f]

[a]*Department of Mathematics, Modelling and Scientific Computing (MOX), Politecnico di Milano, Milan, Italy;* [b]*Laboratory of Biological Structure Mechanics (LaBs), Department of Chemistry, Material and Chemical Engineering, Politecnico di Milano, Milan, Italy;* [c]*Laboratoire Jacques-Louis Lions, Sorbonne Universités, UPMC Univ Paris 06, UMR 7598, F-75005 Paris, France;* [d]*Laboratoire Jacques-Louis Lions, CNRS, UMR 7598, F-75005 Paris, France;* [e]*INRIA-Paris-Rocquencourt, EPC MAMBA, Domaine de Voluceau, BP105, 78153 Le Chesnay Cedex, France;* [f]*Modeling and Scientific Computing (CMCS), MATHICSE, Ecole Polytechnique Fédérale de Lausanne (EPFL), Lausanne, Switzerland*

(*Received 30 January 2014; accepted 29 June 2014*)

Permanent metallic implants, such as dental fillings and cardiac devices, generate streaks-like artefacts in computed tomography (CT) images. In this article, we propose a strategy to perform metal artefact reduction (MAR) that relies on the total variation-H^{-1} inpainting, a variational approach based on a fourth-order total variation (TV) flow. This approach has never been used to perform MAR, although it has been profitably employed in other branches of image processing. A systematic evaluation of the performance is carried out. Comparisons are made with the results obtained using classical linear interpolation and two other partial differential equation-based approaches relying, respectively, on the Fourier's heat equation and on a second order TV flow. Visual inspection of both synthetic and real CT images, as well as computation of similarity indexes, suggests that our strategy for MAR outperforms the others considered here, as it provides best image restoration, highest similarity indexes and for being the only one able to recover hidden structures, a task of primary importance in the medical field.

Keywords: metal artefact reduction; computed tomography; image inpainting; variational and PDE methods

1. Introduction

Metal artefacts represent a serious problem in X-ray computerised tomography (CT), as they are commonly observed in images of patients with permanent metallic implants (e.g. dental fillings, hip prostheses, cardiac devices). They originate from beam hardening, which is due to high X-ray attenuation of the metallic parts and allows only a limited number of photons to reach the CT detectors. The radiation intensities collected by CT detectors are organised, as a function of projection angles and detector positions, into the so-called sinogram matrix. Metal artefacts lead to inconsistent sinogram projections, which alter the image reconstruction process and result in dark streaks surrounded by bright streaks. These artefacts can seriously degrade image quality, especially in the presence of high atomic number metals, such as iron or platinum (Kataoka et al. 2010).

During the past three decades, various approaches have been proposed for reducing artefacts caused by metallic implants. These approaches are generally referred to as metal artefact reduction (MAR) techniques, and they can be *prima facie* classified as iterative reconstruction methods and interpolation-based methods.

Iterative methods operate directly on the original raw sinogram data, and compensate for the missing projections through modified versions of classical iterative reconstruction algorithms. They can be divided into two main groups: algebraic techniques, e.g. algebraic reconstruction and simultaneous iterative reconstruction (Wang et al. 1996; Robertson et al. 1997), and statistical techniques, e.g. maximum likelihood-expectation maximisation algorithms (De Man et al. 2000; Nuyts et al. 1999). The need for original raw sinogram data, which are often unavailable, and the high computational costs represent the major drawbacks of these techniques.

However, interpolation-based methods aim at identifying the corrupted parts of the sinogram and replacing them by using information coming from the uncorrupted neighbouring projections. Usually, these methods are less computationally expensive than the iterative ones, and can be implemented starting from the reconstructed image. As a result, they do not require original raw projection data. They typically consist of four steps: segmentation of metal regions in the native image, forward projection of the image and forward projection of the metal, sinogram restoration and reconstruction of the final image via filtered back projection (FBP). The strategies used to perform the sinogram restoration step include, among others, linear interpolation (LI) (Kalender et al. 1987; Meyer et al. 2010, 2011), cubic interpolation (Bazalova et al. 2007), spline interpolation (Abdoli et al. 2010), wavelet-based interpolation (Zhao et al. 2000) and

*Corresponding author. Email: elena.faggiano@polimi.it

techniques involving either a variational principle, through a minimisation process, or a (non necessarily variational) partial differential equation (PDE) (Duan et al. 2008; Zhang et al. 2011).

The latter techniques rely on the idea that the missing parts of an image can be filled using information diffused from the nearby areas through a suitable PDE. Using the Fourier's heat equation (HE) is the simplest way to diffuse information. However, due to its regularisation property, this equation cannot preserve discontinuous image features. In order to address this shortcoming, suitable nonlinear versions of the HE have been designed, as the ones relying on second order total variation (TV) flow proposed in Shen and Chan (2002), where the diffusivity constant depends upon the size of the image gradient, so that diffusion near edges is namely reduced. Although achieving clear improvements over the HE, these second-order PDEs still have disadvantages, for instance, they do not perform well on edges spanning large gaps, and this has motivated the usage of higher order PDEs for image inpainting. Among fourth-order PDEs, Shen et al. (2003) proposed in 2003 a new variational inpainting method based on the Euler's Elastica (EE), which allows for isophotes connection across large distances. Bertozzi et al. (2007a) introduced in 2007 a new fourth-order method relying on the Chan–Hilliard (CH) equation, which shares the good properties as the EE method and, in addition, it can be solved by fast computational techniques (Bertozzi et al. 2007b). Bertozzi and coworkers proposed in 2009 the total variation-H^{-1} (TV-H^{-1}) method as a possible generalisation of the CH method, conceived for high contrast or binary images, to grey-value images (Burger et al. 2009; Schönlieb et al. 2009). The same fast computational technique developed for the CH method applies to the TV-H^{-1} method as well (Schönlieb and Bertozzi 2011).

Although profitably employed in other branches of image processing, to the best of our knowledge, this variational method has never been used to perform sinogram inpainting. In this article, we propose a strategy to perform MAR that relies on the TV-H^{-1} method.

We organise our article as follows. Section 2 briefly describes variational image inpainting, in general, and the variational method under consideration, in particular. The key features of the performance evaluation procedure are also introduced. Section 3 summarises the results obtained on synthetic data, i.e. six phantom images with metal artefacts, and clinical CT images of patients with metallic implants. The performance of our method is tested through visual inspection and similarity indexes, and it is compared with the performance of LI, HE and TV inpainting methods, which are assumed as standard references. Finally, a critical discussion of the obtained results is provided and some conclusive considerations are drawn in Section 4.

2. Methods

2.1 Variational image inpainting

From a mathematical standpoint, a 2D image can be identified with a domain $\Omega \subset \mathbb{R}^2$ (i.e. the image domain) and a function u^0 mapping the image intensity distribution over Ω. In this framework, the area of the image to be inpainted can be considered as a set $D \subset \Omega$ (i.e. the inpainting domain) and the inpainting problem consists of using the values attained by the function u^0 in $\Omega \backslash D$ to find a distribution u that fills D properly.

The past few years testified, among others, the spreading of variational methods for image inpainting. We refer to Burger et al. (2009) and references therein for a general literature on the subject. Such methods rely on the idea that the solution u of the inpainting problem can be identified with the steady solution of an evolution equation propagating u^0 from $\Omega \backslash D$ into D.

In more detail, given an open and bounded domain Ω with Lipschitz boundary $\partial\Omega$, $u^0(\cdot) \in L^2(\Omega)$ and $u(t,\cdot) \in BV(\Omega)$ for all $t \in \mathbb{R}_+$, solving an image inpainting problem consists of finding the steady state of a PDE in the form given hereafter, provided with initial condition $u(t = 0,\cdot) = u^0(\cdot)$ in Ω and Neumann boundary condition on $\partial\Omega$:

$$\begin{aligned} \partial_t u(t,x) &= \lambda \chi_{\Omega\backslash D}(x)(u^0(x) - u(t,x)) + R(u), \\ &(t,x) \in \mathbb{R}_+ \times \Omega. \end{aligned} \tag{1}$$

Equation (1) can be derived as the Euler–Lagrange equation associated to the following variational problem:

$$\min_{u \in BV(\Omega)} \left\{ \lambda \int_{\Omega\backslash D} |u^0 - u|^2 \, \mathrm{d}x + R_V(u) \right\}. \tag{2}$$

The first term on the right-hand side of (1) keeps memory of the original image. The parameter $\lambda \in \mathbb{R}_+$ is the so-called fidelity parameter and $\chi_{\Omega\backslash D}(\cdot)$ is the characteristic function of the set $\Omega \backslash D$. The term $R(u)$ is a regularising spatial differential operator, whose definition characterises the inpainting method. The order of the inpainting method is identified by the order of (1).

The TV-H^{-1} method proposed in Schönlieb et al. (2009) relies on the following definition:

$$R(u) := \Delta p, \quad p \in \partial TV(u), \tag{3}$$

where $\partial TV(u)$ denotes the subdifferential of the functional $TV(u)$. An element $p \in \partial TV(u)$ can be approximated by a smoothed version of $\nabla\cdot(\nabla u/|\nabla u|)$. For instance, we can use the square root regularisation to achieve

$$R(u) := \Delta\nabla\cdot\left(\frac{\nabla u}{\sqrt{|\nabla u|^2 + \varepsilon^2}}\right), \tag{4}$$

with $0 < \varepsilon \ll 1$. Plugging definition (4) into (1), we obtain the fourth-order PDE representing the TV-H^{-1} inpainting method.

2.2 Fourth order variational MAR procedure

The MAR procedure proposed here relies on the steps summarised in Figure 1, which are briefly described as follows:

A. *Segmentation and removal of metal regions*. The metallic parts of the available image are segmented by means of a threshold method. The segmented areas are then removed to obtain an image free from metal parts.
B. *Projection into the Radon space*. The Radon transform of the image free from the metal parts is computed to obtain the related sinogram.
C. *Sinogram processing*. The obtained sinogram is processed through the TV-H^{-1} inpainting. Briefly, using the same notations introduced in Section 2.1, the subtracted sinogram identifies the image domain Ω and the projection values define the image intensity distribution u^0. The inpainting domain D consists of those areas of the sinogram that correspond to metallic parts (see Figure 2). Then, we solve in Ω the PDE (1) with the definition (4), initial condition u^0, and Neumann boundary conditions. The numerical solution is obtained by using the fast solver proposed by Schönlieb and Bertozzi (2011), which relies on the following unconditionally stable discrete time-stepping scheme:

$$\frac{u_{k+1}-u_k}{\Delta t}+C_1\Delta\Delta u_{k+1}+C_2u_{k+1} = C_1\Delta\Delta u_k-\Delta\nabla\cdot\left(\frac{\nabla u_k}{\sqrt{|\nabla u_k|^2+\varepsilon^2}}\right) + \lambda\chi_{\Omega\setminus D}(x)(u^0-u_k)+C_2u_k, \quad (5)$$

where Δt is the time step, and constants C_1 and C_2 satisfy $C_2 > (2/\varepsilon\pi)$ and $C_2 > \lambda$, respectively (Schönlieb and Bertozzi 2011). In our implementation, we solve Equation (5) in the spectral domain using the discrete cosine transform. The resulting equilibrium distribution u defines the corrected sinogram. Concerning the choice of parameters involved in Equation (5), we note that, when the fidelity parameter, λ, is not selected properly, the images resulting from the MAR procedure are altered, and their quality worsen consequently (see Table 1). However, the parameters ε, C_1 and C_2 play a less active role in the image restoration process. In fact, ε is the parameter related to the square root regularisation of the gradient; as such, it has to be selected sufficiently small. The parameters C_1 and C_2 are proper to the numeric scheme, and they must satisfy the aforementioned conditions.
D. *Sinogram projection and reinsertion of metal image*. The image associated to the corrected sinogram is computed through FBP. The metallic parts initially segmented are then reinserted into the corrected image.

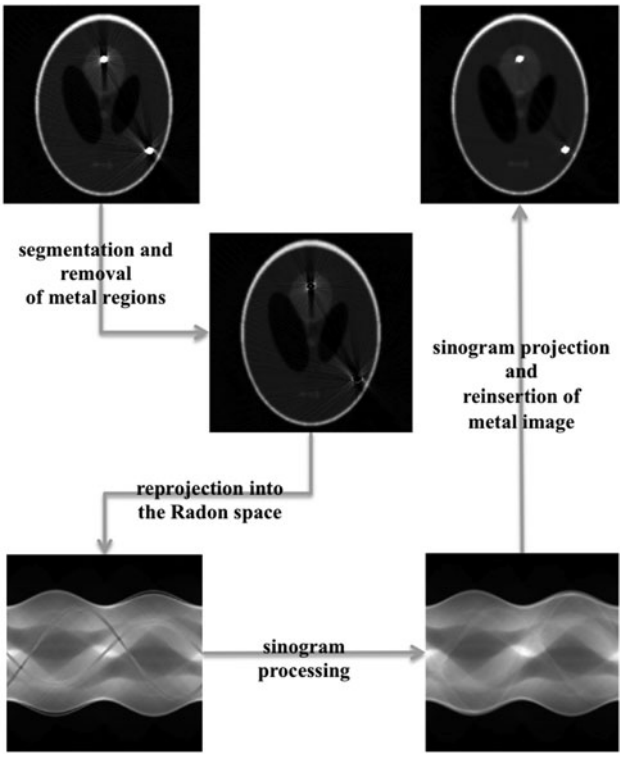

Figure 1. Flowchart of the strategy followed to perform MAR.

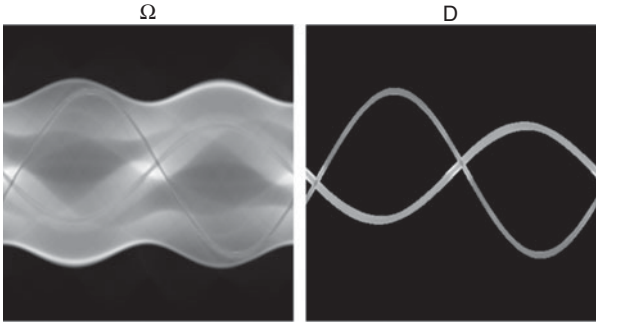

Figure 2. Image domain Ω (left) and inpainting domain D (right).

2.3 Performance evaluation

We apply the proposed method on synthetic data and CT medical images. Next, we compare its performance with that of the LI, HE and TV inpainting methods, which have been selected as standard references.

Table 1. Similarity indexes of the phantom image with five metal regions corrected by means of the MAR procedures relying on the HE, TV and TV-H^{-1} methods for different values of λ.

	Region 2				Region 3				Whole image			
	PSNR	NCC	MSSIM	FSIM	PSNR	NCC	MSSIM	FSIM	PSNR	NCC	MSSIM	FSIM
HE												
$\lambda = 1$	**21.792**	**0.979**	**0.892**	**0.994**	**25.175**	**0.880**	**0.799**	**0.980**	**33.289**	**0.936**	**0.690**	0.969
$\lambda = 10$	20.520	0.973	0.876	0.993	25.112	0.877	0.790	0.980	33.107	0.932	0.681	**0.972**
$\lambda = 100$	20.365	0.977	0.884	0.994	24.733	0.867	0.756	0.975	33.149	0.933	0.665	0.966
TV												
$\lambda = 1$	16.975	0.937	0.756	0.981	24.641	0.863	0.721	0.968	33.187	0.934	0.669	0.966
$\lambda = 10$	**17.006**	**0.938**	**0.757**	0.981	**24.649**	**0.863**	**0.722**	**0.968**	**33.189**	**0.934**	**0.669**	**0.966**
$\lambda = 100$	16.747	0.935	0.756	**0.984**	24.525	0.859	0.719	0.967	33.152	0.933	0.664	0.965
TV-H^{-1}												
$\lambda = 1$	21.569	0.977	0.876	0.982	25.236	0.882	0.826	0.977	32.631	0.925	0.688	**0.975**
$\lambda = 10$	24.556	0.989	0.930	0.994	25.370	0.886	0.856	0.987	33.235	0.935	0.708	**0.975**
$\lambda = 100$	**25.674**	**0.992**	**0.943**	**0.996**	**25.384**	**0.887**	**0.858**	**0.987**	**33.324**	**0.936**	**0.710**	0.972

Note: The highest values are indicated in boldface.

2.3.1 *Synthetic data*

We generate six Shepp–Logan phantoms of 256×256 pixels with one to six metal regions of high attenuation and induced artefacts. As highlighted by the first panel of Figure 3, three significant regions of the phantom are identified, which are used for performance evaluation. Region 3 includes metal parts and the majority of the areas affected by metal artefacts. However, Regions 1 and 2 contain little objects that we aim at preserving and enhancing with the MAR procedure. In particular, Region 1 contains an ellipse, partially superimposed on another bigger ellipse, which is made nearly invisible by metal artefacts.

Four similarity indexes are computed in Regions 2 and 3, and on the whole image as well, to evaluate performance: the peak-signal-to-noise ratio (PSNR), the normalised cross-correlation coefficient (NCC), the Mean Structural SIMilarity (MSSIM) index and the Feature SIMilarity (FSIM) index. All these indexes are extensively used in image processing to validate, or evaluate, the results of different methods (Zhang et al. 2011; Kratz et al. 2012).

The PSNR is defined as

$$\mathrm{PSNR}(X, Y) := 10 \times \log_{10}\left(\frac{X_M^2}{\|Y(\cdot) - X(\cdot)\|^2_{L^2(\Gamma)}}\right), \quad (6)$$

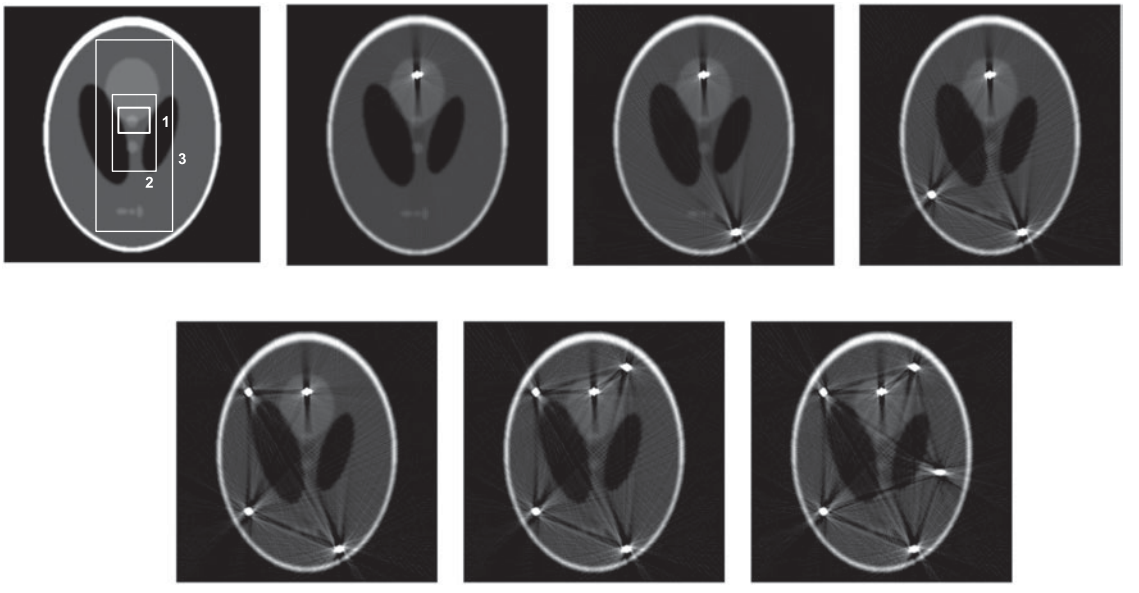

Figure 3. Shepp–Logan phantoms used for performance evaluation. From left to right, from top to bottom, image of the original phantom where the specific areas that we use to evaluate the results are highlighted, and images of the phantoms with metal induced artefacts.

where $X_M = \max X$, the function Y stands for the intensity distribution of the artefact corrected image, the function X is the intensity distribution of the reference image (i.e. the original image without metal artefacts), and $\Gamma \subset \mathbb{R}^2$ is the related image domain. The higher the PSNR value, the better the performance of the method.

The NCC is defined as

$$\mathrm{NCC}(X,Y) := \frac{1}{|\Gamma|}\int_\Gamma \frac{(Y(x)-\mu_Y)(X(x)-\mu_X)}{\sigma_Y\sigma_X}\,\mathrm{d}x, \quad (7)$$

where μ_Y and μ_X are, respectively, the average values of the intensity distributions Y and X, while σ_Y and σ_X are the related standard deviations. The NCC is equal to 1 if the following identity holds:

$$Y(x) = X(x) \quad \forall x \in \Gamma.$$

The MSSIM index is given by

$$\begin{aligned}\mathrm{MSSIM}(X,Y) &:= \frac{1}{M}\sum_{j=1}^{M}\mathrm{SSIM}(x_j,y_j),\\ \mathrm{SSIM}(x,y) &:= \frac{(2\mu_x\mu_y + C_1)(2\sigma_{xy}+C_2)}{(\mu_x^2+\mu_y^2+C_1)(\sigma_x^2+\sigma_y^2+C_2)},\end{aligned} \quad (8)$$

where X and Y are the reference and the corrected image, x_j and y_j are the image contents in a j-th local window, M is the number of windows, μ_x and μ_y are the local mean intensities, σ_x and σ_y are the standard deviations and σ_{xy} is the correlation coefficient. For the constants C_1 and C_2, we use the same values proposed by the authors in Wang et al. (2004), i.e. $C_1 = (K_1L)^2$ and $C_2 = (K_2L)^2$, with L the dynamic pixel range, $K_1 = 0.01$ and $K_2 = 0.03$. The higher the MSSIM value, the better the performance of the method.

Finally, we compute the FSIM index, which is a feature based image quality index defined as

$$\begin{aligned}\mathrm{FSIM}(X,Y) &:= \frac{\sum_{\mathbf{x}\in\Omega} S_L(\mathbf{x})\cdot PC_m(\mathbf{x})}{\sum_{\mathbf{x}\in\Omega} PC_m(\mathbf{x})},\\ PC_m(\mathbf{x}) &:= \max(PC_X(\mathbf{x}), PC_Y(\mathbf{x})),\end{aligned} \quad (9)$$

where $PC_X(\mathbf{x})$ and $PC_Y(\mathbf{x})$ are the phase congruency values computed in each pixel $\mathbf{x}$ of the reference and corrected image, respectively. For more details about the definition of the phase congruency (see Zhang et al. 2011). Moreover,

$$S_L(\mathbf{x}) := S_{PC}(\mathbf{x})\cdot S_G(\mathbf{x}) \quad (10)$$

is the local feature similarity index with

$$\begin{aligned}S_{PC}(\mathbf{x}) &:= \frac{2PC_X(\mathbf{x})\cdot PC_Y(\mathbf{x}) + T_1}{PC_X(\mathbf{x})^2 + PC_Y(\mathbf{x})^2 + T_1} \quad \text{and}\\ S_G(\mathbf{x}) &:= \frac{2G_X(\mathbf{x})\cdot G_Y(\mathbf{x}) + T_2}{G_X(\mathbf{x})^2 + G_Y(\mathbf{x})^2 + T_2},\end{aligned} \quad (11)$$

where $G_X(\mathbf{x})$ and $G_Y(\mathbf{x})$ are the magnitude of the gradients in each pixel $\mathbf{x}$ of the reference and corrected image, respectively. The constants T_1 and T_2 are fixed as proposed by Zhang et al. (2011).

2.3.2 *Clinical data*

Two head-neck CT images of a patient with dental fillings and two chest CT images of a patient with a pacemaker are used to evaluate the performance of the MAR methods considered here. Images are 512×512 pixels, with pixel size equal to $0.976\,\mathrm{mm} \times 0.976\,\mathrm{mm}$ for the head-neck images and $0.43\,\mathrm{mm} \times 0.43\,\mathrm{mm}$ for the chest images. Evaluations are performed through visual inspection of the CT scans and the profile-lines of the attenuation coefficients related to some representative probing lines (Meyer et al. 2010; Chen et al. 2012).

3. Results

Simulations are performed in MATLAB 64 bit (R2011b, The MathWorks, Natick, MA, USA) on a 2.27 GHz Intel (R) Core i5 processor, with 3.7 GB RAM.

3.1 *Synthetic data*

We focus first on the phantoms shown in Figure 3. Simulations of the HE, TV methods and the proposed fourth-order variational TV-H^{-1} method are run, respectively, for 1000, 10,000 and 1000 iterations to allow the related PDEs to reach the steady state. The computational costs of the methods are reported in Table 3. The value of the fidelity parameter λ is set equal to 1 for the HE method, 10 for the TV method and 100 TV-H^{-1} method. These values have been selected after some trials in order to guarantee the best possible results for each method. Table 1 summarises the values of the similarity indexes computed on the image with five metal regions for different values of λ. Similar trends have been obtained for the other images. As could be seen in Table 1, the highest values are obtained with $\lambda = 1$ for the HE method, $\lambda = 10$ for the TV method and $\lambda = 100$ for the TV-H^{-1} method.

As a matter of example, the results related to the phantom with four metal objects are reported in Figure 4. Similar results have been obtained in the cases of the other phantoms summarised in Figure 3. Panel OI refers to the phantom without metal artefacts, while Panel PA shows the phantom containing metal artefacts. Panels from LI to TV-H^{-1} display the corrected images, which result from the MAR procedures relying on the four inpainting methods under consideration. This figure shows how metal artefacts are suppressed to different extents. The TV-H^{-1} inpainting method achieves better visual effects compared with the LI, HE and TV inpainting methods.

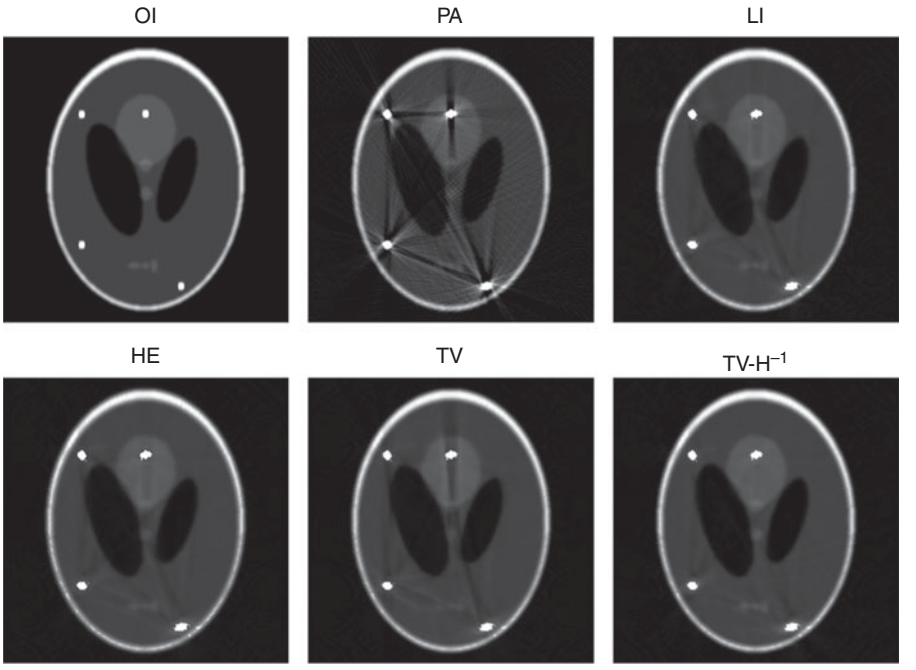

Figure 4. Phantom with four metal objects. From left to right, from top to bottom, the original image (OI), the image containing metal artifacts (PA) and the corrected images of the MAR procedures relying on the LI, HE, TV and TV-H^{-1} methods.

In fact, the results of the TV-H^{-1} method are smoother and characterised by less marked residual artefacts. However, the other three methods provide a substantial metal artefact reduction, but they maintain more evident residual artefacts in the surrounding of the metallic objects.

Turning to the analysis of Region 1, the higher performance of the TV-H^{-1} method in preserving and recovering image information can be further appreciated. In particular, Figure 5 supports the idea that our MAR procedure relying on the TV-H^{-1} method allows to recover hidden structures. In fact, a little ellipse on a non-uniform background is visible in the Region 1 of the reference image, while this is totally absent in the image with the metal artefacts. The same ellipse becomes again distinguishable

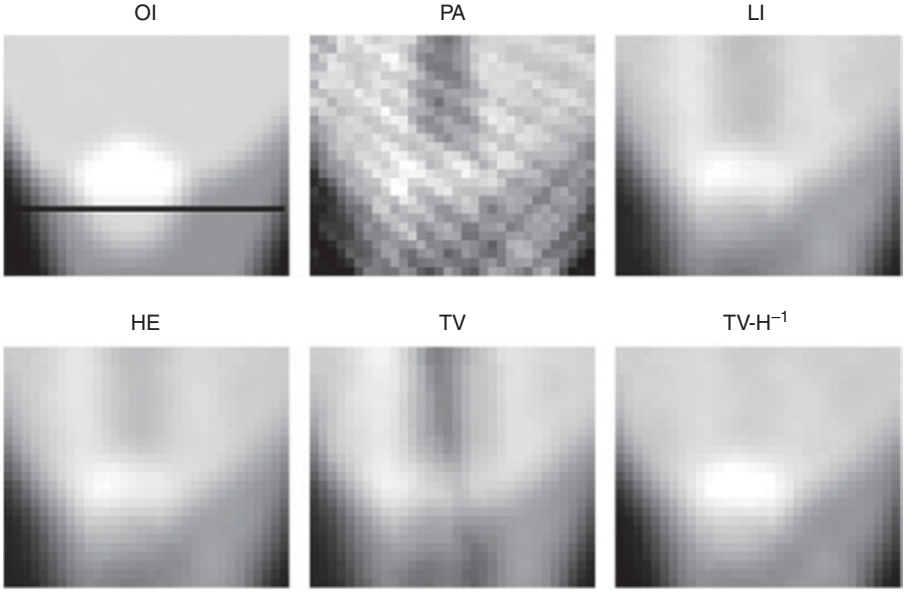

Figure 5. Region 1 of the phantom with four metal objects. From left to right, from top to bottom, the original image (OI), the image containing metal artifacts (PA) and the corrected images of the MAR procedures relying on the LI, HE, TV and TVH^{-1} methods. The black line in Panel OI highlights the reference line used for the comparisons reported in Figure 6.

after TV-H^{-1} inpainting of the sinogram, while the other methods considered here are not able to restore such a structure, probably because of its proximity to the metallic object. The worst results are obtained with the TV method. These considerations become even more evident if we look at Figure 6, where a significant profile-line of the attenuation coefficient is reported for each one of the six images in Figure 5. The selected reference line is highlighted by the black line in Panel OI of Figure 5. The curve without markers refers to the original image, while the dashed curve refers to the image with artefacts. We can distinguish three parts in the reference curve: a first one referring to the black area, a second one with an attenuation value around 0.3, which is the small ellipse, and a third one with attenuation around 0.2. Looking at the pattern of the TV-H^{-1} data, it takes the same values as the ones of the original image in the first and third areas, and a value very close to the original one in the part corresponding to the small ellipse. Moreover, the shape of the TV-H^{-1} profile line is very similar to the one of the original image without artefacts. The behaviours of the LI and HE methods are similar: they underestimate the value in the second area and overestimate the value in the third area. Moreover, despite the original data, their profiles in the second area are not constant.

The above-mentioned considerations are also confirmed by the values attained by the similarity indexes (see Table 2) in Regions 2 and 3 and in the whole image. In fact, the highest values of PSNR, NCC, MSSIM and FSIM are obtained with the TV-H^{-1} method for each one of the six phantoms, in particular in Regions 2 and 3 where important features are present. It is worth noting that the values related to the LI and HE methods, although smaller than that related to the TV-H^{-1} method, are still higher than that of the image with metal artefact. This indicates a good restoration quality. Finally, the lowest values are obtained by using the TV method, and they are close to the values of the image with metal artefacts.

3.2 Clinical data

With reference to clinical data, simulations related to the HE, TV methods and the proposed fourth-order variational TV-H^{-1} method are run, respectively, for 10,000, 1000 and 1000 iterations to allow the related PDEs to reach the steady state. The computational costs for each method are reported in Table 3. On the line of the considerations drawn in Section 3.1, the value of the fidelity parameter λ is set equal to 1 for the HE method, 10 for the TV method and 100 for the TV-H^{-1} method.

The obtained results are summarised in Figures 7–10, where Panel OI shows the original image with dark and board streaks radiating from metallic implants. Panels from LI to TV-H^{-1} illustrate the results obtained with the LI, HE, TV methods and the proposed fourth-order variational TV-H^{-1} method. In order to further appreciate the modifications introduced by the MAR methods, one representative profile-line of the attenuation coefficient is shown for each image (see white solid lines) in the same figure. Metallic implants and bones result into high picks, while dark-band artefacts correspond to concavities with lower attenuation coefficients.

Figures 7–10 show how dark streaks are corrected by all methods, although some residual artefacts still remain in the proximity of metallic implants. Looking at the profile-lines, frequent small changes in the attenuation coefficient dominate the profiles related to the LI method. Such changes are reduced in the profiles related to the other methods at hand. In particular, the profile-lines shown in Panel TV-H^{-1} are smoother than the others, and concavities with lower attenuation coefficients are much

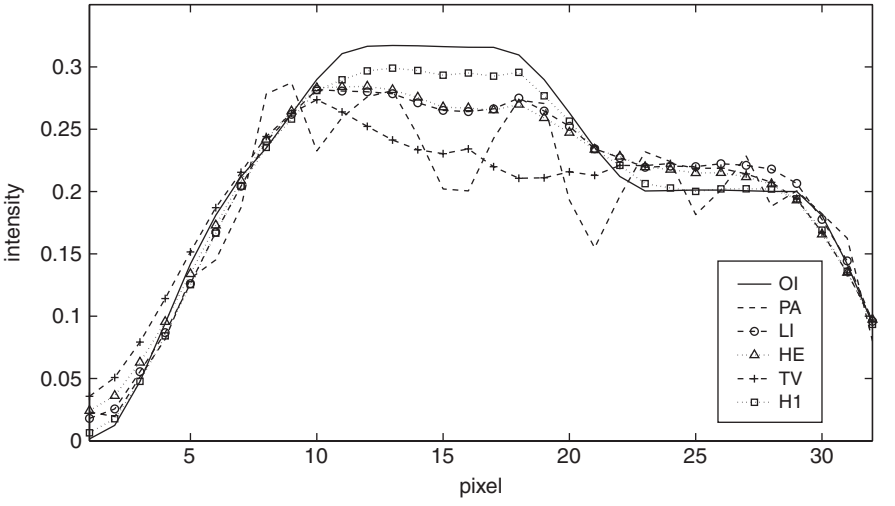

Figure 6. Region 1 of the phantom with four metal objects. Profile-lines of the attenuation coefficient for the original image (OI), the image containing metal artifacts (PA) and the corrected images obtained with the MAR procedures relying on the LI, HE, TV and TV-H^{-1} methods. The selected reference line is highlighted by the black line in Panel OI of Figure 5.

Table 2. Similarity indexes of the image containing metal artefacts (PA) and the images corrected by means of the MAR procedures relying on the LI, HE, TV and TV-H^{-1} methods.

	Region 2						Region 3						Whole image					
	1	2	3	4	5	6	1	2	3	4	5	6	1	2	3	4	5	6
PSNR																		
PA	22.57	19.61	18.74	18.19	17.54	17.46	26.20	24.36	23.90	23.89	22.42	22.19	32.98	35.29	33.37	32.56	32.01	31.08
LI	24.51	21.52	21.33	21.66	19.84	19.87	28.27	26.74	26.70	27.23	25.06	25.00	33.43	36.18	34.44	33.78	33.28	32.45
HE	24.23	21.88	21.67	21.93	21.79	20.50	28.21	26.75	26.70	27.23	25.17	25.06	32.09	35.85	34.21	33.58	33.29	32.31
TV	19.77	17.93	17.76	18.18	17.01	16.98	27.54	26.13	26.07	26.58	24.65	24.56	32.82	36.02	34.33	33.68	33.19	32.37
TV-H^{-1}	**29.63**	**26.59**	**26.31**	**26.66**	**25.67**	**25.61**	**28.44**	**26.98**	**26.95**	**27.52**	**25.38**	**25.32**	**33.44**	**36.20**	**34.46**	**33.81**	**33.32**	**32.49**
NCC																		
PA	0.980	0.967	0.950	0.933	0.928	0.905	0.898	0.849	0.831	0.826	0.791	0.776	0.989	0.952	0.933	0.923	0.916	0.903
LI	0.987	0.976	0.975	0.978	0.966	0.968	0.932	0.907	0.905	0.915	0.876	0.873	**0.991**	**0.961**	**0.947**	**0.941**	**0.936**	0.927
HE	0.988	0.982	0.981	0.982	0.979	0.975	0.930	0.906	0.904	0.915	0.880	0.875	0.987	0.958	0.943	0.938	0.936	0.925
TV	0.958	0.947	0.945	0.952	0.938	0.937	0.918	0.892	0.889	0.901	0.863	0.859	0.989	0.959	0.945	0.939	0.934	0.926
TV-H^{-1}	**0.997**	**0.994**	**0.994**	**0.994**	**0.992**	**0.992**	**0.936**	**0.912**	**0.911**	**0.921**	**0.887**	**0.884**	**0.991**	**0.961**	**0.947**	**0.941**	**0.936**	**0.928**
MSSIM																		
PA	0.92	0.85	0.72	0.62	0.61	0.55	0.88	0.70	0.59	0.50	0.42	0.37	**0.95**	0.72	0.60	0.53	0.49	0.45
LI	0.92	0.88	0.88	0.88	0.86	0.86	0.93	0.86	0.83	0.82	0.77	0.76	0.93	0.81	0.74	0.71	0.69	0.66
HE	0.92	0.90	0.89	0.89	0.89	0.88	0.93	0.87	0.84	0.83	0.80	0.78	0.92	0.80	0.73	0.70	0.69	0.65
TV	0.82	0.79	0.78	0.79	0.76	0.75	0.87	0.80	0.77	0.76	0.72	0.71	0.92	0.79	0.72	0.69	0.67	0.64
TV-H^{-1}	**0.97**	**0.96**	**0.95**	**0.95**	**0.94**	**0.94**	**0.96**	**0.92**	**0.89**	**0.88**	**0.86**	**0.83**	0.94	**0.82**	**0.76**	**0.73**	**0.71**	**0.68**
FSIM																		
PA	0.994	0.989	0.981	0.968	0.965	0.950	0.986	0.968	0.961	0.949	0.932	0.922	**0.986**	0.959	0.953	0.945	0.943	0.940
LI	0.995	0.993	0.993	0.994	0.991	0.992	0.993	0.988	0.985	0.985	0.976	0.975	0.974	0.972	0.970	0.968	0.968	0.966
HE	0.995	0.995	0.995	0.995	0.994	0.993	0.993	0.989	0.986	0.986	0.980	0.979	0.978	**0.976**	**0.974**	0.970	0.969	**0.971**
TV	0.989	0.985	0.984	0.986	0.981	0.982	0.986	0.982	0.978	0.979	0.968	0.967	0.973	0.971	0.969	0.967	0.966	0.965
TV-H^{-1}	**0.998**	**0.997**	**0.998**	**0.997**	**0.996**	**0.997**	**0.996**	**0.992**	**0.990**	**0.989**	**0.987**	**0.985**	0.976	**0.976**	**0.974**	**0.971**	**0.972**	**0.971**

Notes: Numbers from 1 to 6 refer to phantoms with one to six metal regions. The highest values are indicated in boldface.

Table 3. Computational times expressed in seconds of the MAR procedures relying on the LI, HE, TV and TV-H^{-1} methods.

	Synthetic data						Clinical data			
	1	2	3	4	5	6	Head-neck 1	Head-neck 2	Chest 1	Chest 2
LI	0.94	1.21	0.94	1.01	0.97	1.01	3.55	1.33	3.51	4.32
HE	59.04	67.15	66.71	66.29	65.56	63.30	658.47	660.92	655.33	660.26
TV	1345.81	1452.86	1471.72	1456.13	1466.97	1447.41	115.80	88.71	124.49	121.10
TV-H^{-1}	90.25	91.42	98.62	99.89	98.59	97.18	89.86	88.71	120.77	122.71

Note: Numbers from 1 to 6 refer to phantoms with one to six metal regions.

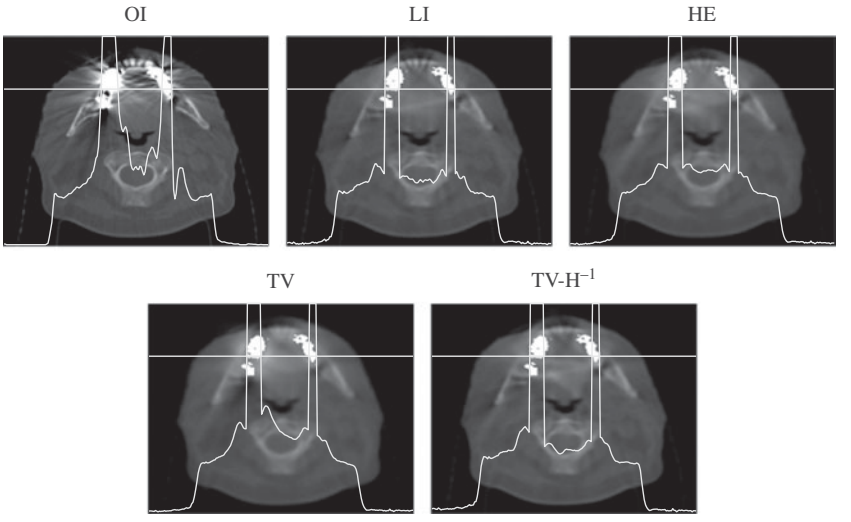

Figure 7. Head-neck CT image 1. From left to right, from top to bottom, the original image containing metal artefacts (OI) and the corrected images of the MAR procedures relying on the LI, HE, TV and TV-H^{-1} methods. White solid lines show the profile of the attenuation coefficient related to the highlighted profile line.

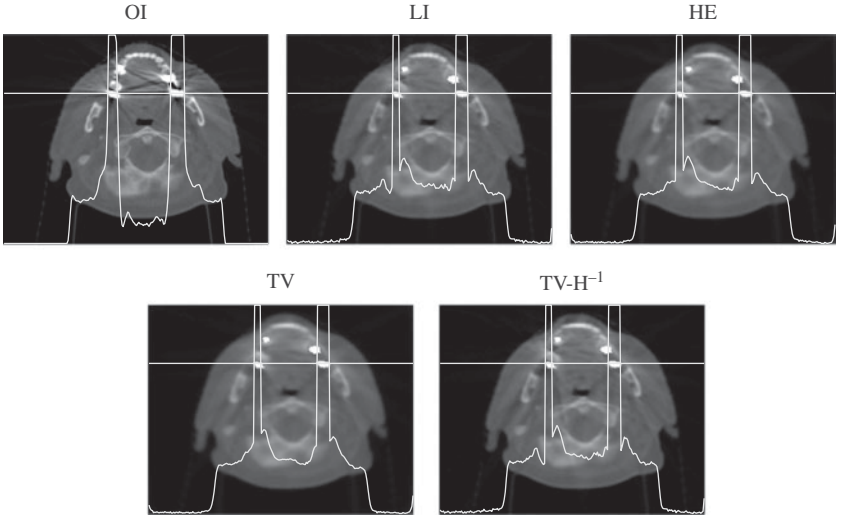

Figure 8. Head-neck CT image 2. From left to right, from top to bottom, the original image containing metal artefacts (OI) and the corrected images of the MAR procedures relying on the LI, HE, TV and TV-H^{-1} methods. White solid lines show the profile of the attenuation coefficient related to the highlighted profile line.

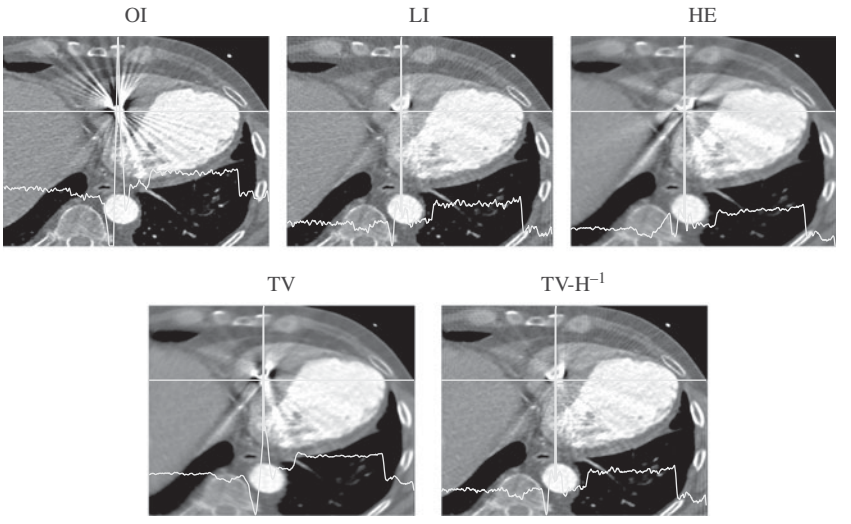

Figure 9. Chest CT image 1. From left to right, from top to bottom, the original image containing metal artefacts (OI) and the corrected images of the MAR procedures relying on the LI, HE, TV and TV-H^{-1} methods. White solid lines show the profile of the attenuation coefficient related to the highlighted profile line.

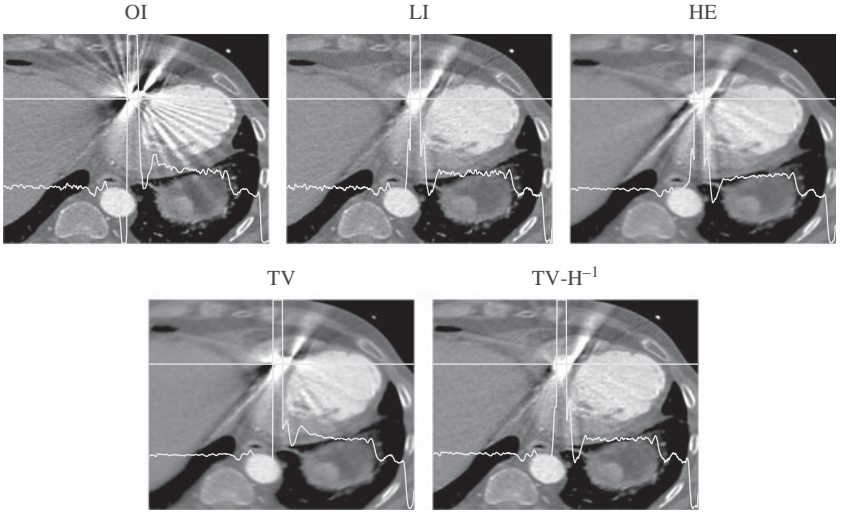

Figure 10. Chest CT image 2. From left to right, from top to bottom, the original image containing metal artefacts (OI) and the corrected images of the MAR procedures relying on the LI, HE, TV and TV-H^{-1} methods. White solid lines show the profile of the attenuation coefficient related to the highlighted profile line.

less evident. For instance, in Figure 10 Panel TV-H^{-1}, we can appreciate how the profile of the image intensity is constant, apart from some small fluctuations, in the areas that are expected to be characterised by a homogeneous intensity distribution (e.g. at the level of the ventricle). The profile-line related to the TV method is also smooth, but it appears to attain wrong values.

4. Discussion and conclusion

A promising way to reduce artefacts caused by permanent metallic implants in CT images is provided by interpolation-based methods, which aim at identifying the corrupted parts of the sinogram and replacing them by using information coming from uncorrupted neighbouring projections.

The fourth-order variational method relying on the TV-H^{-1} inpainting equation was profitably employed in other branches of image processing (Bertozzi et al. 2007b; Burger et al. 2009; Schönlieb et al. 2009), but it has never been used before to perform sinogram inpainting. This method allows a smooth connection of wide inpainting regions and it can be solved with a fast solver.

Moving from these considerations, we have proposed a new strategy for MAR based on the TV-H^{-1} inpainting equation, and we have compared its performance with the ones of the LI, HE and TV inpainting methods, which have been selected as standard references.

Dealing with synthetic images, our analysis relied both on visual inspection and similarity index calculations, since original data free from metal artefacts are known. In more detail, we have first compared the results of the methods at hand in terms of PSNR, NCC, MSSIM and FSIM, which have been evaluated on significant regions of the image (see Tables 1 and 2). These indexes had already been used before in this kind of application (Zhang et al. 2011; Kratz et al. 2012). Then, in order to test the capabilities of our method in preserving and restoring structural information, we have compared a profile line of the attenuation coefficient traversing a small region in the processed images (see Figures 5 and 6). The results reported are an indicator of the ability of our MAR strategy to recover hidden structures and to preserve morphological information, which are tasks of primary importance in the medical field.

Conversely, analysis developed on real CT scans relied on visual inspections, which involved also the profile of the attenuation coefficient related to an explicative probing line as in Chen et al. (2012) and Meyer et al. (2010).

Preservation and substantial improvement of the information content related to synthetic data is achieved by all methods at hand. In fact, they are able to reduce dark strikes due to metal artefacts and to enhance the proposed similarity indexes. The worst results have been obtained with the TV method, while the performances of the LI and HE methods are comparable. The TV-H^{-1} method outperforms the others providing highest similarity indexes, best image restoration and being the only one able to recover hidden structures (see Figures 5 and 6). This is also suggested by the results related to clinical data (see Figures 7–10), where profile lines confirm the supremacy of the TV-H^{-1} method in correcting metal artefacts and restoring regions with uniform grey values. The results obtained support the idea that the HE and TV methods are less effective than the fourth-order variational method at hand, at least to perform sinogram inpainting, as we could expect since they rely on second-order PDEs.

With respect to computational costs, the LI method is the fastest method: it takes maximum 4 s to perform the restoration of a large clinical image. The time taken using the TV-H^{-1} method ranges from 90 s to a maximum of 120 s on a standard laptop. Given that the code was implemented in MATLAB without any specific optimisation, this appears to be a reasonable computational cost. The other two methods (HE and TV) are characterised by variable computational times, ranging from a minimum of 59 s (HE on phantom with one metal artefact) to a maximum of 1470 s (TV on phantom with three metal artefacts).

In conclusion, on the basis of the results presented here and the considerations drawn earlier, we support the usage of this fourth-order variational method for MAR. Future researches will aim at further investigating the performance of this method using additional CT scans of patients with metallic implants, as well as at designing segmentation algorithms more accurate than the threshold method used here. Furthermore, the performance of the TV-H^{-1} method can be compared with the performance of more accurate interpolation-based methods, as the one presented by Joshi et al. (2011). Finally, as an additional research perspective, we believe that the performance of our MAR procedure can be improved by adding a further step that combines the results of the TV-H^{-1} inpainting together with the original sinogram data, namely through a procedure as that proposed by Meyer et al. (2011, 2012).

Acknowledgements

The work of E.F. was supported by the European Research Council Advanced Grant Mathcard, Mathematical Modelling and Simulation of the Cardiovascular System Project ERC-2008-AdG 227058. The work of T.L. was supported by the Fondation Sciences Mathématiques de Paris (FSMP), by a public grant overseen by the French National Research Agency (ANR) as part of the *Investissements d'Avenir* program (reference: ANR-10-LABX-0098) and the FIRB project – RBID08PP3J.

References

Abdoli M, Ay MR, Ahmadian A, Dierckx R, Zaidi H. 2010. Reduction of dental filling metallic artifacts in CT-based attenuation correction of PET data using weighted virtual sinograms optimized by a genetic algorithm. Med Phys. 37 (12):6166–6177.

Bazalova M, Beaulieu L, Palefsky S, Verhaegen F. 2007. Correction of CT artifacts and its influence on Monte Carlo dose calculations. Med Phys. 34(6):2119–2132.

Bertozzi AL, Esedoglu S, Gillette A. 2007a. Inpainting of binary images using the Cahn–Hilliard equation. IEEE Trans Image Process. 16(1):285–291.

Bertozzi AL, Esedoglu S, Gillette A. 2007b. Analysis of a two-scale Cahn–Hilliard model for binary image inpainting. Multiscale Model Simul. 6(3):913–936.

Burger M, He L, Schönlieb CB. 2009. Cahn–Hilliard inpainting and a generalization for gray value images. SIAM J Imaging Sci. 2(4):1129–1167.

Chen Y, Li Y, Guo H, Hu Y, Luo L, Yin X, Gu J, Toumoulin C. 2012. CT metal artifact reduction method based on improved image segmentation and sinogram in-painting. Math Probl Eng. 2012:1–18.

De Man B, Nuyts J, Dupont P, Marchal G, Suetens P. 2000. Reduction of metal streak artifacts in X-ray computed tomography using a transmission maximum a posteriori algorithm. IEEE T Nucl Sci. 47(3):977–981.

Duan X, Zhang L, Xiao Y, Cheng J, Chen Z, Xing Y. 2008. Metal artifact reduction in CT images by sinogram TV inpainting. In: IEEE nuclear science symposium conference record, 2008 (NSS'08). Dresden (Germany): IEEE; p. 4175–4177.

Joshi S, Marquina A, Osher S, Dinov I, Toga A, Horn JV. 2011. Fast edge-filtered image upsampling. In: IEEE international

conference on image processing (ICIP). Vol. 18. Brussels (Belgium): IEEE; p. 1165–1168.
Kalender WA, Hebel R, Ebersberger J. 1987. Reduction of CT artifacts caused by metallic implants. Radiology. 164(2):576–577.
Kataoka ML, Hochman MG, Rodriguez EK, Lin PJP, Kubo S, Raptopolous VD. 2010. A review of factors that affect artifact from metallic hardware on multi-row detector computed tomography. Curr Probl Diagn Radiol. 39(4):125–136.
Kratz B, Weyers I, Buzug TM. 2012. A fully 3D approach for metal artifact reduction in computed tomography. Med Phys. 39(11):7042–7054.
Meyer E, Raupach R, Lell M, Schmidt B, Kachelrieß M. 2010. Normalized metal artifact reduction (NMAR) in computed tomography. Med Phys. 37:5482–5493.
Meyer E, Raupach R, Lell M, Schmidt B, Kachelrieß M. 2012. Frequency split metal artifact reduction (FSMAR) in computed tomography. Med Phys. 39:1904–1916.
Meyer E, Raupach R, Schmidt B, Mahnken AH, Kachelrieß M. 2011. Adaptive normalized metal artifact reduction (ANMAR) in computed tomography. In: 2011 IEEE nuclear science symposium and medical imaging conference (NSS/MIC). Valencia (Spain): IEEE; p. 2560–2565.
Nuyts J, De Man B, Dupont P, Defrise M, Suetens P, Mortelmans L. 1999. Iterative reconstruction for helical CT: a simulation study. Phys Med Biol. 43(4):729–737.
Robertson DD, Yuan J, Wang G, Vannier MW. 1997. Total hip prosthesis metal-artifact suppression using iterative deblurring reconstruction. J Comput Assist Tomogr. 21(2):293–298.
Schönlieb CB, Bertozzi A. 2011. Unconditionally stable schemes for higher order inpainting. Commun Math Sci. 9(2):413–457.
Schönlieb CB, Bertozzi A, Burger M, He L. 2009. Image inpainting using a fourth-order total variation flow. In: SAMPTA'09, international conference on sampling theory and applications.
Shen J, Chan TF. 2002. Mathematical models for local nontexture inpaintings. SIAM J Appl Math. 62(3):1019–1043.
Shen J, Kang SH, Chan TF. 2003. Euler's elastica and curvature-based inpainting. SIAM J Appl Math. 63(2):564–592.
Wang G, Snyder DL, O'Sullivan J, Vannier M. 1996. Iterative deblurring for CT metal artifact reduction. IEEE Trans Med Imaging. 15(5):657–664.
Wang Z, Bovik AC, Sheikh HR, Simoncelli EP. 2004. Image quality assessment: from error visibility to structural similarity. IEEE Trans Image Process. 13(4):600–612.
Zhang L, Zhang D, Mou X. 2011. FSIM: a feature similarity index for image quality assessment. IEEE Trans Image Process. 20(8):2378–2386.
Zhang Y, Pu YF, Hu JR, Liu Y, Chen QL, Zhou JL. 2011. Efficient CT metal artifact reduction based on fractional-order curvature diffusion. Comput Math Methods Med. 2011:1–9.
Zhao S, Robeltson D, Wang G, Whiting B, Bae KT. 2000. X-ray CT metal artifact reduction using wavelets: an application for imaging total hip prostheses. IEEE Trans Med Imaging. 19(12):1238–1247.